Data-Driven Bayesian Optimization Framework for Rapidly Developing Novel Wideband, Low-Profile Dipole Antenna with 3D Printed Technology

Sun, Ying; Zhang, Jin; Tibo, Alessandro; Aghabeyki, Peyman; Wei, Zhaohui; Luo, Shengyuan; Zhang, Shuai

Published in:
IEEE Transactions on Antennas and Propagation

DOI (link to publication from Publisher):
10.1109/TAP.2024.3490836

Publication date:
2025

Document Version
Accepted author manuscript, peer reviewed version

Data-Driven Bayesian Optimization Framework for Rapidly Developing Novel Wideband, Low-Profile Dipole Antenna with 3D Printed Technology

Ying Sun, Jin Zhang, Alessandro Tibo, Peyman Aghabeyki, Zhaohui Wei, Shengyuan Luo, and Shuai Zhang, *Senior Member, IEEE*

***Abstract*—This paper presents an innovative framework for fast-developing broadband, low-profile, dual-polarized cross-dipole antennas. This approach integrates a broadband, petal-shaped cross dipole with a 3D-printed structure comprising multi-layers of high permittivity material with varying heights and radii. In the absence of a theoretical model and a satisfactory initial design, the design process employs the enhanced Tree-structured Parzen Estimator Bayesian Optimization (TPE-BO) algorithm, a significant advancement over traditional Bayesian methods, for effective hyper-parameter tuning to streamline the design. The proposed method only adjusts the high dielectric constant loading (HDL) structure without changing the original dimensions of the dipole. Compared to conventional optimization algorithms integrated within CST, this method efficiently achieves the desired broadband and low profile performance. Meanwhile, the mechanism of the HDL structure in increasing the bandwidth (BW) while enabling the dipole's low profile performance is explained. The proposed approach has been validated by fabricating and measuring a hybrid antenna prototype. The measured results show that the antenna achieves an overlap BW between the impedance matching BW and the 3 dB gain BW of 79.3% (from 1.62 to 3.75 GHz) with a voltage standing wave ratio (VSWR) of less than 1.6. Additionally, the isolation between the two ports exceeds 20.5 dB. Significantly, this HDL technique notably enhances the BW and reduces the antenna's profile from $0.2\lambda_L$ to $0.1\lambda_L$ compared to a single petal-shaped cross dipole. Thus, this study provides a simple, effective, and repeatable design strategy for realizing broadband and low profile performance in dipole antennas.**

***Index Terms*—Acquisition function, bayesian optimization, dipole antenna, design exploration, low profile, tree-structured parzen estimator, wideband antenna.**

I. Introduction

RAPID advances in modern wireless communications and radar technologies have greatly increased interest in broadband and low-profile antenna research. Meanwhile, the role of dual-polarized antennas in increasing channel capacity is becoming increasingly important as spectrum resources become more limited [1]. At the same time, the trend towards more compact and integrated systems is making broadband antennas with minimal profiles more attractive to designers. Valued for their adaptability, low-profile antennas have a wide range of applications in wireless communications [2], conformal arrays [3], wearable technology [4] and antenna-in-package solutions [5]. Consequently, to meet the growing need for higher data rates in the face of limited spectrum availability and the demand for smaller, integrated systems, the development of broadband, low-profile, dual-polarized antennas is crucial for the continued advancement of wireless communication technology.

Various dipole antennas with excellent impedance matching have been investigated to meet the demands for wide bandwidth (BW) capabilities [6]–[12]. A common approach involves incorporating parasitic elements into the dipole [10], [11]. For instance, adding four parasitic resonator patches at the top and a broadband hybrid ring coupler at the bottom resulted in a 42.4% impedance BW with a voltage standing wave ratio (VSWR) of less than 1.6 [11]. Similarly, integrating a parasitic patch and a convex-shaped reflector achieved a 64.7% BW with a VSWR of $\leq$ 1.5 [10]. However, these designs introduce new scattering sources due to the parasitic elements around or above the radiator. Additionally, the need for an extra decoupling network results in larger volumes.

Another method of BW enhancement is the magneto-electric (ME) dipole antenna, which combines electric and magnetic dipoles to ensure BW, optimal realized gain, and low cross-polarization [8], [9], [12]. For instance, [9] achieved a BW of 3-4.5 GHz with a VSWR of $\leq$ 1.5, but this approach involves complex manufacturing processes. To further extend the BW while reducing the profile, artificial magnetic conductors (AMC) and metasurfaces have been used instead of traditional perfect electric conductor (PEC) reflectors [8], [12], achieving profiles of $0.09\lambda_L$ and $0.12\lambda_L$ with increased overall dimensions and complexity. While integrating various structures into a dipole antenna enhances BW and reduces profile, it inevitably affects the intrinsic performance of the dipole antenna. Therefore, optimizing performance requires not only adjusting additional components but also modifying the dipole antenna's structure and dimensions to ensure good impedance matching and BW. This process complicates the design and extends development time.

This paper proposes a novel approach for extremely broadening the BW and simultaneously reducing the profile of a

Manuscript received 5 April 2024 (Corresponding author: Shuai Zhang).

Ying Sun, Jin Zhang, Peyman Aghabeyki, and Shuai Zhang are with the Antennas, Propagation and Millimeter-wave Systems (APMS) section, Department of Electronic Systems, Aalborg University, 9220 Aalborg, Denmark (e-mail: yisu@es.aau.dk; jzhang@es.aau.dk; pag@es.aau.dk; sz@es.aau.dk).

Alessandro Tibo is with the Computer Science Department, Aalborg University, 9220 Aalborg, Denmark (e-mail: alessandro@cs.aau.dk).

Zhaohui Wei is with the Key Laboratory of Antennas and Microwave Technology, Xidian University, Xi'an 710071, China. (e-mail: zhaohui_wei@163.com).

Shengyuan Luo is with the College of Electronic and Information Engineering, Anhui University, Anhui 230601, China. (e-mail: 24713@ahu.edu.cn).

cross dipole antenna only by high dielectric constant loading (HDL) structure without changing the original dipole structure, simply by adjusting the height and radius of the HDL structure. However, due to the significant impact of variations in HDL height and radius on antenna BW (see Sec. II), given the impracticality of the traditional methods such as trial and error, parameter sweeping, and local optimization, exploring a global optimization approach is essential to obtain the optimal geometric parameters that achieve the desired performance.

Antenna optimization is widely recognized as a nonconvex black-box problem due to the complex interactions between the antenna's physical parameters and performance metrics [13]–[15]. Consequently, traditional gradient-based optimization algorithms often fail to solve these problems because gradient information is typically unavailable in most antenna optimizations [14]–[17]. Therefore, this paper employs an advanced global optimization method for complex multidimensional problems (exceeding 20 design parameters) [18]: the Tree-structured Parzen Estimator Bayesian Optimization (TPE-BO) algorithm. TPE-BO, a refinement of traditional Bayesian Optimization (BO), quickly identifies the optimal geometric parameters [19], [20]. Unlike traditional optimization algorithms such as Trust Region Framework (TRF) [13], [21], Particle Swarm Optimization (PSO) [22], [23], which directly target the optimization objective function, TPE-BO constructs a surrogate model based on non-parametric distribution model [15], [17], [19], [20]. This model guides the search for the optimal solution by balancing exploration and exploitation of the high-dimensional hyper-parameter space [17], [19]. This method is highly effective for addressing expensive black-box optimization problems, rapidly converging without requiring a large amount of simulated EM data [17], [24]. Compared to conventional BO, TPE-BO facilitates multidimensional optimization and achieves rapid convergence [19], [20]. To the best of the authors' knowledge, this is the first introduction of TPE-BO algorithms in antenna BW optimization.

The remainder of this paper is organized as follows: Section II introduces the proposed petal-shaped cross-dipole structure and analyzes the principle of the HDL structure for profile reduction while improving wideband performance. Section III details the TPE-BO algorithm and the optimization process. Section IV presents the performance of the optimized broadband antenna (measured results), and Section V concludes the paper.

II. Antenna Configuration and Working Mechanism

The proposed low profile broadband antenna integrates a 3D-printed HDL structure, depicted in Fig. 1. It comprises a radiating patch printed on the bottom of the substrate1, an HDL structure, two coaxial cables, a metal reflector, and four plastic posts above the reflector. Detailed views of the HDL structure and the radiating patch layer are presented separately in Fig. 2.

As shown in Fig. 2(a), the radiating patch layer consists of two pairs of identical vertical irregular petal-shaped cross dipoles printed on the bottom layer of a Rogers RO4350B

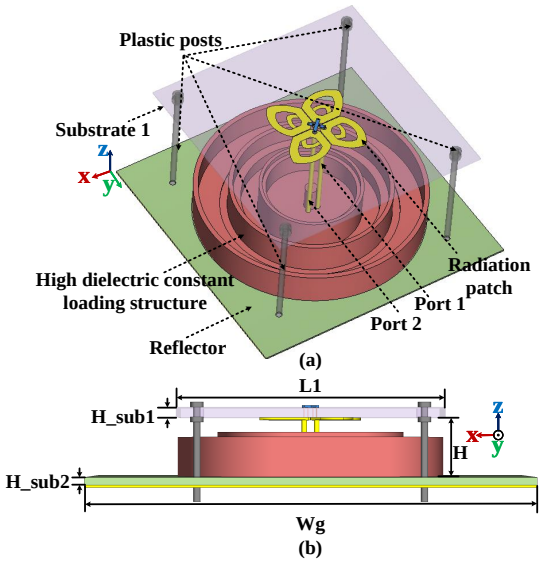

Fig. 1. Configuration of the proposed 3-D printed antenna with HDL structure: (a) 3-D view, and (b) side view. Specifications: H = 18.27 mm, H_sub1 = 0.762 mm, H_sub2 = 0.762 mm, W_g = 195 mm.

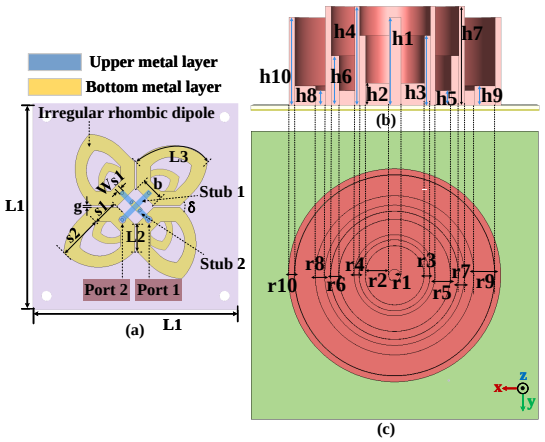

Fig. 2. The detailed geometry of the proposed antenna. (a) Top view of the radiating layer, (b) cross-sectional view of the HDL structure, and (c) top view of the HDL structure. Specifications: $L_1 = 108.8$, $g = 0.33$, $W_{s1} = 1.6$, $b = 4.3$, $s_1 = 9$, $s2 = 15$, all in millimeters. Size of HDL is shown in Table I.

substrate with ε_r = 3.66, a loss tangent of 0.0037, and a thickness H_sub1 = 0.762 mm to achieve $\pm 45^{\circ}$ polarization. The coaxial cable directly feeds two pairs of crossed dipoles. Port 1 for $+45^{\circ}$ polarization and Port 2 for -45° polarization. Additionally, the outer conductors of the two coaxial cables are soldered separately to one arm of each pair of irregular petal-shaped dipoles. Two microstrip stubs 1 and 2 connected to coaxial cables are introduced for impedance matching. One side of stub 1, printed on the top of substrate1, is connected to the inner conductor of the coaxial cables, and the other side of stub 1 is connected to the half dipole via a metallic hole in substrate1. Notably, the middle portion of stub 2 is printed on the bottom of substate1 to prevent physical overlap of the two stubs, and the two ends of stub 2 are connected to the dipole via the two metallic holes in substrate1.

Beneath the substrate1, a 3D-printed HDL structure, com-

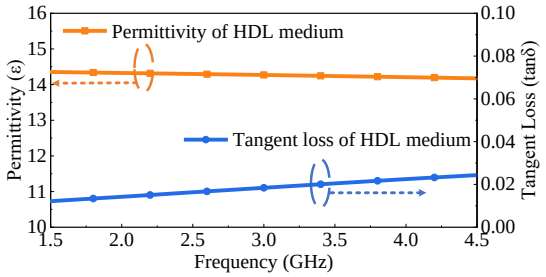

Fig. 3. The performance of HDL medium.

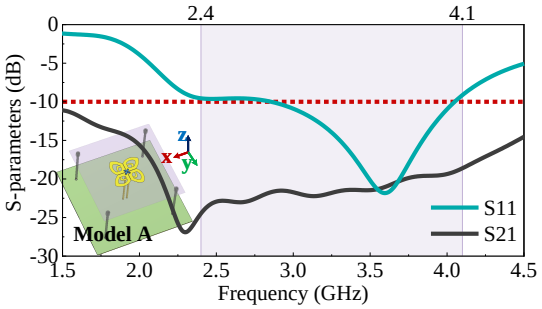

Fig. 4. S-parameters of the single petal-shaped antenna without HDL.

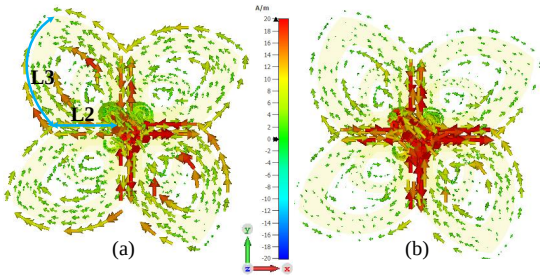

Fig. 5. Top view of the current distribution of Model A. (a) 2.4 GHz, and (b) 3.6 GHz.

posed of 10 layers of dielectric rings with different radii and heights, as illustrated in Fig. 2(b) and (c). This HDL, made of a special ABS-based compound, offers a stable dielectric constant (ε_r = 15, loss tangent = 0.018) over a wide range of frequencies and temperatures with relatively low loss. It is suitable for both extrusion and injection molding, making it ideal for the complex and broadband structure of the antenna [25]. To align the simulation results with practical testing, the structure was measured using the DAK-TL2, a tool that quickly and accurately characterizes the dielectric constant of materials with limited thickness (0.1 – 10 mm) that are available in sheet form [26]. As depicted in Fig. 3, the dielectric constant ranges from 14.2 ± 0.2 over 1-6 GHz, with a tangent loss of almost 0.018. The dielectric constant of the simulation was adjusted from the nominal 15 to the actual 14.2 to ensure congruence between the simulated and actual conditions.

The antenna's reflector, made of copper soldered onto FR-4 with an ε_r of 4.4, a loss tangent of 0.02, and a thickness of 0.762 mm. The size of the reflector is 195 mm × 195 mm. Due to the symmetrical structure design, the antenna's performance is nearly identical at both ports. Therefore, the following studies and simulations in this paper, conducted using the commercial electromagnetic field simulation software, CST STUDIO SUITE (CST), will only focus on port 1.

A. Dual-band Antenna Operation Mechanism

First, a wideband dipole antenna, Model A, with a petal shape is introduced, as shown in Fig. 4. Model A exhibits two effective resonances at 2.4 and 3.6 GHz. As illustrated in Fig. 5, at 2.4 GHz, the current is concentrated along the entire edge of the dipole, with the resonance frequency controlled by the L2 and L3. At 3.6 GHz, the current is mainly distributed in the slot between the dipole elements, with resonance point mainly controlled by L2.

Verification by parameter studies, as shown in Fig. 6, shows that the 2.4 GHz resonance is correlated with variations in L2 and L3, indicating an electrical dipole resonance. In contrast, variations in L3 have minimal impact on the 3.6 GHz resonance, which is therefore primarily determined by the slot dimensions L2 between the dipole elements. In addition, this antenna BW is correlated with L2, L3, and height H. Increasing the values of L2 and L3 results in wider BW, and increasing H improves both impedance matching and BW.

For this study, we mainly propose a framework that effectively and quickly improves BW and impedance matching

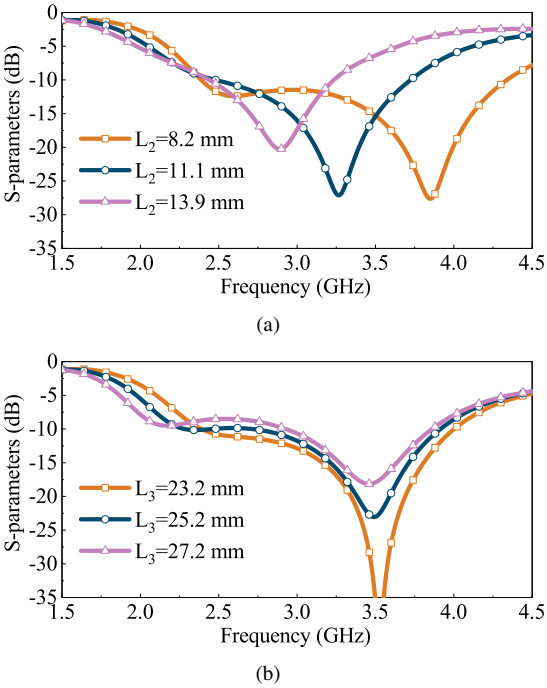

Fig. 6. Simulated S_{11} of Model A by (a) changing the value of L2 and (b) changing the value of L3.

without altering the size or structure of the original dipole antenna. This is achieved by combining an HDL structure and a global optimization algorithm (described in the following sections). Therefore, here we would like to use a relatively basic dipole example with a compact structure, providing a dual-resonance mode, to verify the effectiveness and universality of the proposed framework. The dipole used in this framework can also be replaced by other compact dual-resonance mode

dipole antennas. The S-parameter of this petal-shaped antenna, which has a return loss greater than 10 dB between 2.4 GHz and 4.1 GHz with a total profile height of 0.154 λ_L (where λ_L is the wavelength at the lowest frequency of Model A), is shown in Fig. 4.

B. Development of a Low-Profile Antenna Incorporating HDL Technology

Common knowledge in antenna design dictates that the profile of a dipole antenna is typically limited to 0.25 wavelength to achieve in-phase radiation. This limitation compensates for the 180° reflection phase difference caused by the ground plane. Therefore, to reduce the profile height of the dipole antenna, the integration of an HDL structure at its bottom is proposed, which compensates for the phase while maintaining optimal performance. As detailed in (1), the total height H of the dipole antenna needs to satisfy the following condition to achieve a zero phase difference between the direct radiation electric field and the electric field reflected from the ground.

$$\frac{2\pi}{\lambda_g} \times 2H = 2k\pi \,(k = 0, \pm1, \pm2, \dots)\,, \tag{1}$$

$$\lambda_g = \frac{2\pi}{\beta}. \tag{2}$$

where λ_g is the dielectric wavelength of electromagnetic waves in a medium, and H is the distance between the dipole antenna and the ground. According to the theories of electromagnetic wave propagation referred to [27], the relationship between the phase constant β and the permittivity of the medium ε is as follows:

$$\beta \simeq \omega\sqrt{\mu\varepsilon}\left\{\frac{1}{2}\left[\left(1+\frac{1}{2}\left(\frac{\sigma}{\omega\varepsilon}\right)^2\right)+1\right]\right\}^{1/2} = \omega\sqrt{\mu\varepsilon}. \tag{3}$$

where ω is the angular frequency, μ the permeability of a medium, and σ is the conductivity of the medium. Substituting (2) and (3) into (1) gives a direct relationship between profile height and permittivity that can be used directly to guide the design of a low-profile dipole framework.

$$2H\omega\sqrt{\mu\varepsilon} = 2k\pi \,(k = 0, \pm1, \pm2, \dots)\,. \tag{4}$$

Analysis of (4) reveals an inverse relationship between the height H of the dipole antenna and the permittivity ε. As the permittivity of the material increases, the profile height of the antenna decreases. However, it is worth noting that the permittivity cannot be increased indefinitely. Although using high-permittivity materials can effectively reduce the overall size of the antenna, increasing the permittivity significantly decreases high-frequency radiation efficiency. This decrease indicates that the antenna's ability to convert input power into radiated electromagnetic waves is reduced, confining more energy within the high permittivity structure [28]. Consequently, higher Q-factors reduce the impedance BW of the dipole antenna, making it challenging to achieve low-profile and broadband performance. To achieve wideband while maintaining a compact structure, it is necessary to introduce additional resonance points.

C. Enhancing BW Performance with HDL Structure Integration

As references [29]–[33] indicated, the incorporation of dielectric material can achieve a compact structure while simultaneously functioning as a dielectric resonator antenna (DRA) when appropriately designed. Model B is formed by loading an HDL structure with a height of 5 mm and a radius of 70 mm directly underneath Model A, as illustrated in Fig. 7. This modification reduces the lowest operating frequency of the antenna from 2.4 GHz to 2.1 GHz, demonstrating the effective profile reduction achieved by the HDL structure. Moreover, incorporating the HDL introduces additional resonances (forming by DRA mode). Consequently, the initial two resonant modes of the dipole are expanded to four, thus enabling broadband performance.

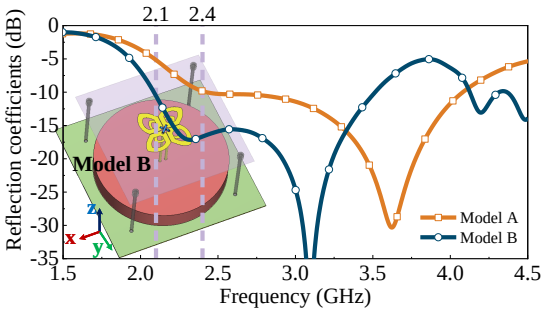

Fig. 7. S-parameters of the single petal-shaped antenna and petal-shaped antenna with single layer HDL structure.

The DRA can excite multiple radiation modes [29] [30] [32]. The radiation mode and operating frequency of the cylindrical DRA antenna are mainly influenced by its radius, equivalent dielectric constant, and the ratio of radius to height (r/h). These effects are nonlinear [29] [33]. As illustrated in Fig. 8, the excitation of the dielectric resonance (DR) mode necessitates a specific condition. When the height of the HDL in Model B is 3mm, even with a substantial variation in the radius, the DR mode will not be excited, and the hybrid antenna still maintains the original two modes of the dipole. However, when the DR radiation mode is excited, changes in radius and height affect both the number of DR modes and their corresponding frequencies, as well as the equivalent permittivity of the loaded HDL. This, in turn, impacts the operating frequency band and matching of the original dipole mode, as illustrated in Fig. 9.

To effectively excite the DR mode, common methods include stacking multiple DRAs or combining materials with different permittivities [29] [32]. This variation in permittivity induces controlled relaxation of field confinement, allowing electromagnetic waves to propagate more freely from the dielectric resonator to the surrounding air. Additionally, different permittivities alter the working modes of the dielectric resonator, changing the field distribution inside the dielectric material, which makes it easier to excite the more DR modes [32]. However, these methods are complex to manufacture.

Therefore, this paper proposes a multi-layer circular ring stack structure of varying heights, as illustrated in Fig. 1, introducing air gaps to create this permittivity variation. This

structure is simple to manufacture (only by 3D printing technology), effectively excites the multiple DR modes, and provides flexibility and freedom for impedance matching adjustments. By reasonably controlling the height and radius of the circular rings to adjust the position and size of the air gaps, achieving dynamic adjustment of the equivalent permittivity, working mode and corresponding working frequency band of the hybrid antenna, the resonant frequencies of the dipole's two modes and the DR's multiple modes can be merged, forming a multi-resonant characteristic and compact structure, thereby achieving a good broadband design.

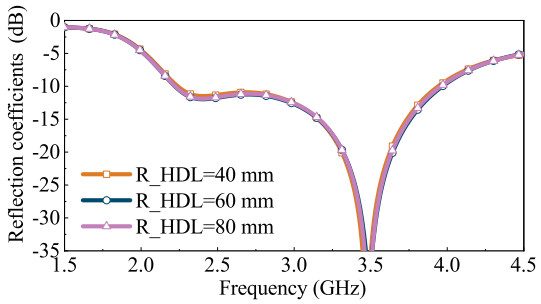

Fig. 8. Reflection coefficients of Model B with different radii when H_HDL = 3 mm.

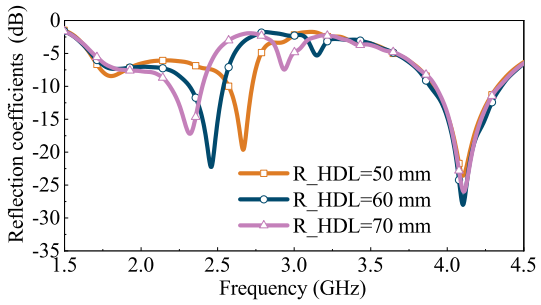

(a)

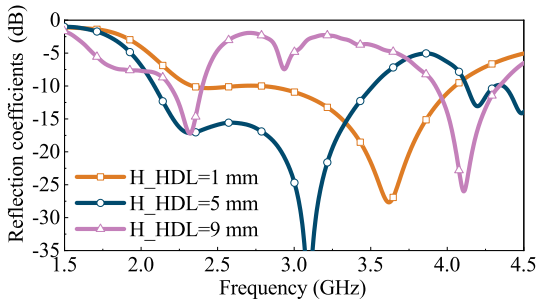

(b)

Fig. 9. Reflection coefficients of Model B with varying heights and radii of HDL when DR modes are excited. (a) H_HDL = 9 mm, and (b) R_HDL = 70 mm.

To effectively excite multiple DR modes while considering the feasibility of manufacturing (our design aims to keep the overall size of the HDL structure within 0.6λ, where λ is the wavelength at the lowest operating frequency), we designed the multi-layer circular ring structure with ten layers of different heights and radii. This approach aims to explore a wide range of resonance modes and impedance matching combinations to improve BW performance and achieve a low profile. However, a large number of highly relevant design parameters (20 for this design) are generated. These design parameters affect not only the resonance position but also the operating mode (i.e., number of resonances and radiation pattern) and impedance matching of the antenna. Finding an optimal parameter combination among these highly correlated variables, which successfully excites multiple DR modes and ensures effective coupling between the DR and dipole modes for good impedance matching, is a highly challenging task. Traditional methods such as parameter sweeping and trial-and-error are often insufficient and particularly time-consuming. Therefore, a data-driven global optimization strategy is necessary to effectively explore the design space and navigate the complex variable landscape, as discussed in Section III.

III. Data-Driven Assisted Design Framework and Exploration

This section introduces the TPE-BO method [19], [20], a popular hyperparameter optimization algorithm, and its application to automated antenna design, namely tuning the parameters of the proposed low-profile wideband antenna.

A. Optimization Problem Formulation

An antenna is modeled as a mapping $A : \mathcal{X} \times \mathbb{R}^n \to \mathcal{Y}$, where $\mathcal{X}$ denotes the set of antenna parameters selected by the designer, $\mathbb{R}^n$ denotes the space of adjustable parameters, and $\mathcal{Y}$ denotes the space of observed quantities associated with the antenna. The optimization problem is to find the best set of adjustable parameters with respect to a scalar function $f : \mathcal{Y} \to \mathbb{R}$, called the evaluation function. The optimization problem is formulated as

$$\begin{aligned} \min_{\boldsymbol{x}\in\mathbb{R}^n} \quad & f(A(\cdot,\boldsymbol{x})) \\ \text{s.t.} \quad & \boldsymbol{x}_l \le \boldsymbol{x} \le \boldsymbol{x}_u, \end{aligned} \tag{5}$$

where $f(\boldsymbol{x})$ is the evaluation function, $\boldsymbol{x_l}$ and $\boldsymbol{x_r}$ represent the lower and upper bounds for the adjustable parameters.

For the antenna optimization (parameter tuning) problem, the evaluation function $f(\boldsymbol{x})$ can be return loss, VSWR, broadside gain, coupling, efficiency, polarization, etc. In this study, the optimization objective focuses on enhancing the BW performance within a specified frequency range. Although the introduction of an HDL structure is to activate various modes to achieve wideband, the broadside mode is the desired operational mode in this paper. Consequently, the evaluation function in this research is designed to minimize the total deviations of S_{11} and S_{21} from their respective thresholds and keep the antenna radiating in the broadside direction. The optimization objective function f is the sum of three different

functions, namely, $f(\boldsymbol{x}) = f_1(\boldsymbol{x}) + f_2(\boldsymbol{x}) + f_3(\boldsymbol{x})$, where $f_1(\boldsymbol{x})$, $f_2(\boldsymbol{x})$ and $f_3(\boldsymbol{x})$ are defined as

$$\begin{cases} f_1(\boldsymbol{x}) = \sum_{\omega=\omega_1}^{\omega_2} \max((g_{S11}(\boldsymbol{x},\omega) - T_{S11}), 0), \\ f_2(\boldsymbol{x}) = \sum_{\omega=\omega_1}^{\omega_2} \max((g_{S21}(\boldsymbol{x},\omega) - T_{S21}), 0), \\ f_3(\boldsymbol{x}) = \sum_{\omega=\omega_1}^{\omega_2} \max((T_{gain} - g_{gain}(\boldsymbol{x},\omega)), 0), \end{cases} \tag{6}$$

where $f_1(\boldsymbol{x})$, $f_2(\boldsymbol{x})$, and $f_3(\boldsymbol{x})$ serve as the optimization functions for S_{11}, S_{21}, and realized gain, respectively. The quantities $g_{S11}(\boldsymbol{x},\omega)$, $g_{S21}(\boldsymbol{x},\omega)$, and $g_{gain}(\boldsymbol{x},\omega)$ denote the linearized values of S_{11}, S_{21}, and realized gain at the frequency ω, which are influenced by the geometric parameters $\boldsymbol{x}$. The predetermined thresholds for S_{11}, S_{21}, and realized gain are represented by T_{S11}, T_{S21}, and T_{gain}, respectively. The frequencies ω_1 and ω_2 define the boundaries of the considered frequency band. Consequently, the objective function $f(\boldsymbol{x})$ seeks to minimize the aggregate deviations of $g_{S11}(\boldsymbol{x},\omega)$ and $g_{S21}(\boldsymbol{x},\omega)$ from their corresponding thresholds T_{S11} and T_{S21}, as well as the deviation of $g_{gain}(\boldsymbol{x},\omega)$ from T_{gain}, over the BW $[\omega_1,\omega_2]$.

Note that the function $f(\boldsymbol{x})$ is nonconvex to the set of adjustable parameters $\boldsymbol{x}$. Specifically, equation (6) consists of subfunctions $f_1(\boldsymbol{x})$, $f_2(\boldsymbol{x})$, and $f_3(\boldsymbol{x})$. $f_1(\boldsymbol{x})$ is related to the reflection coefficient $g_{S11}(\boldsymbol{x},\omega)$. The relationship between antenna parameters (structural dimensions and material properties) and performance metrics (like S_{11}, S_{21}, etc.) is typically complex and non-linear, often lacking explicit analytical expressions. Thus, $g_{S11}(\boldsymbol{x},\omega)$ is generally recognized as a nonconvex function [14] [15] [16] [17]. Although the max function is convex, the combination of a non-convex function $g_{S11}(\boldsymbol{x},\omega)$ with a convex function max is generally not convex. Similarly, $f_2(\boldsymbol{x})$ and $f_3(\boldsymbol{x})$ are also non-convex for the same reasons. Consequently, the cost function in equation (6), which is the combination of three non-convex subfunctions, is generally recognized as non-convex. Thus, traditional approaches, which would likely get stuck in local minima, are not available to solve the proposed problem (5). Moreover, solving (5) requires massive electromagnetic (EM) computations of $f_1(\boldsymbol{x})$, $f_2(\boldsymbol{x})$, and $f_3(\boldsymbol{x})$ by a full-wave antenna simulator (CST or HFSS), which is particularly time-consuming. Hence, to address this challenge, an effective and fast global optimization algorithm are implemented to assist design.

It is important to note that all subsequent optimizations utilize 20 design parameters, analyzed through the Time-Domain Finite Integration Technique (FIT) with an accuracy of -40 dB. This structure is discretized in CST with a density of 35 hexahedral grids per wavelength, resulting in 21,373,400 unit grids. On a workstation equipped with a 16-core 3.29 GHz CPU, 382.6 GB RAM, and a 32 GB Tesla V100-PCIE GPU, the average completion time for each full-wave simulation is approximately 13 minutes. The primary optimization objective is to maximize the BW within the 1.65 to 4.1 GHz spectrum, ensuring that the maximum in-band reflection coefficient

TABLE I
SEARCH SPACE UTILIZED BY ALL ALGORITHMS AND OPTIMAL STRUCTURAL PARAMETERS ACHIEVED VIA THE TPE-BO ALGORITHM (UNIT: MM)

DESCRIPTION	PARAM.	SPACE	OPTIMUM
HEIGHT: FIRST LAYER	h_1	[14.4,17.6]	16
HEIGHT: SECOND LAYER	h_2	[1.62,1.98]	1.8
HEIGHT: THIRD LAYER	h_3	[13.95,17.05]	15.5
HEIGHT: FORTH LAYER	h_4	[16.2,18.2]	18
HEIGHT: FIFTH LAYER	h_5	[1.35,1.65]	1.5
HEIGHT: SIXTH LAYER	h_6	[8.1,9.9]	9
HEIGHT: SEVENTH LAYER	h_7	[16.2,18.2]	18
HEIGHT: EIGHTH LAYER	h_8	[2.43,2.97]	2.7
HEIGHT: NINTH LAYER	h_9	[3.15,3.85]	3.5
HEIGHT: TENTH LAYER	h_{10}	[13.5,16.5]	16
RADIUS: FIRST LAYER	r_1	[0.45,3.5]	3
RADIUS: SECOND LAYER	r_2	[16,18.2]	17.8
RADIUS: THIRD LAYER	r_3	[1.62,1.98]	1.8
RADIUS: FORTH LAYER	r_4	[1.8,4.2]	2
RADIUS: FIFTH LAYER	r_5	[5.5,8.5]	8
RADIUS: SIXTH LAYER	r_6	[3.6,4.4]	4
RADIUS: SEVENTH LAYER	r_7	[0.8,2.5]	2
RADIUS: EIGHTH LAYER	r_8	[3,4]	3.5
RADIUS: NINTH LAYER	r_9	[9.45,11.55]	10.5
RADIUS: TENTH LAYER	r_{10}	[0.9,3]	2.3

remains at or below -13 dB and the coupling between two ports does not exceed -20 dB. In addition, the optimization aims for a realized gain in the broadband direction of at least 1 dBi (ensuring that the excited coupling modes radiate in the broadside direction, filtering out undesired DR modes, or reducing the intensity of the undesired modes in the coupling mode), all within the constraints of the key design parameters outlined in Table I, where optimization variables are $\boldsymbol{x} = \{h_1, \cdots, h_{10}, r_1, \cdots, r_{10}\}$. All optimizations were conducted on the specified workstation.

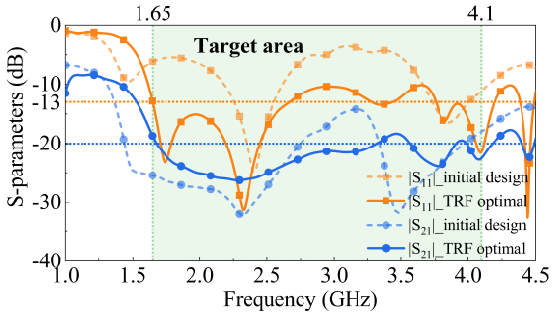

Fig. 10. The optimal results from TRF-based antenna optimization algorithm.

To reduce the computational cost, nearly 50 EM simulations were performed according to the empirical design of the antenna, and one set of parameters within these 50 EM simulations was selected as the initial design $\boldsymbol{x_0}$ for the algorithm we used in this paper. For a black-box function problem in this article, it is difficult to derive or estimate an initial design with reasonably good quality. Without a satisfactory initial design, the TRF algorithm suitable for local optimization is unlikely to obtain a parameter combination that satisfies all requirements in our design. The TRF algorithms were employed three times in CST, utilizing the same initial design depicted in Fig. 10 for verification. Despite utilizing

a larger sigma value to mitigate the risk of converging to a local optimum, the resultant design still converges to a local optimum, manifesting performance well below expectations. Table II presents the optimal design obtained from the three optimization runs, demonstrating that the TRF algorithm is impractical for this wideband antenna design. This highlights the need to incorporate advanced hyper-parameter optimization techniques for more comprehensive design exploration.

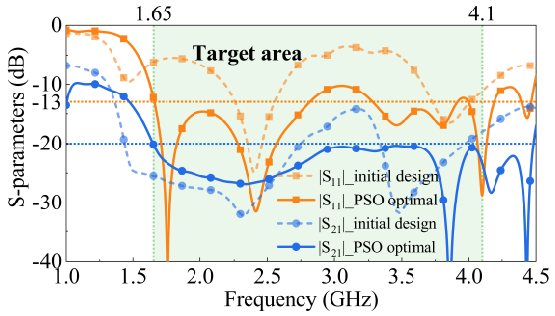

Fig. 11. The optimal results from PSO-based antenna optimization algorithm.

PSO is a heuristic hyper-parameter optimization algorithm inspired by swarm intelligence, widely applied in the field of antenna design exploration [23], [13]. The algorithm's effectiveness is notably affected by the size of the particle swarm. A larger swarm size facilitates extensive search space exploration but incurs higher computational costs. Consequently, there is a need to balance the convergence speed of the algorithm with its accuracy. In our research, the swarm size was set to 50 particles, under a computational limit of 1200 electromagnetic (EM) simulations; all other algorithm settings followed the default configurations in CST. Given the substantial evaluation time exceeding 15 minutes for each iteration and the total duration of a complete PSO cycle exceeding 10 days, the algorithm was executed twice. However, neither attempt yielded satisfactory designs, as demonstrated in Table II, which shows the best design obtained in both runs. This highlights the need to integrate advanced data-driven global optimization techniques. Consequently, this study employs the TPE-BO method to explore satisfactory parameter combinations.

B. TPE-BO Algorithm and Optimization Framework

The TPE-BO algorithm, introduced in this article, is one of the popular and effective algorithms in hyperparameter optimization [19], [20]. To the best of the authors' knowledge, its application in antenna optimization remains uncommon. Typically, a BO algorithm comprises three essential elements: 1) surrogate models, 2) acquisition functions, and 3) optimization metric function [19], [20]. Surrogate models are probabilistic approximations of the black-box function $f(\boldsymbol{x})$, which are usually achieved by the Gaussian Process (GP) model or its variants. Meanwhile, acquisition functions are probability functions used to select (predict) subsequent input point $\boldsymbol{x}$ for evaluation. Optimization metric functions are the optimization objectives designed.

1) Surrogate Model: Surrogate models are commonly used in optimization algorithms [13] [15] [19] [34] and simulation-based design [35] [36]. In optimization algorithms, surrogate models assist in solving complex or black-box optimization problems. In simulation-based design, surrogate models are typically used to reduce or replace direct simulations (such as electromagnetic simulations for antenna design) or expensive experiments. Generally, there are mainly four types of surrogate models: Gaussian process regression [15], radial basis functions [34], neural networks [35], and polynomial regression [36]. In this paper, Gaussian process-based surrogate models inherent in TPE-BO algorithms are introduced to approximate the objective function, instead of fitting a digital model to replace the EM simulation through a large amount of data, making the optimization process more efficient, especially for expensive-to-evaluate or black-box functions.

Unlike traditional BO, the TPE-BO algorithm uses two surrogate models to improve the optimization strategy: one for better-performing observations and the other for worse-performing observations, which are built by kernel density estimators (KDEs). These surrogate models are described as

$$p(\boldsymbol{x} \mid f, \mathcal{D}) = \begin{cases} p\left(\boldsymbol{x} \mid \mathcal{D}^{(l)}\right) & (f \leq f^{\gamma}), \\ p\left(\boldsymbol{x} \mid \mathcal{D}^{(g)}\right) & (f > f^{\gamma}), \end{cases} \tag{7}$$

where $\mathcal{D} = \{(\boldsymbol{x}_i, f_i)\}_{i=1}^{N}$ is a set of observations ($N = |\mathcal{D}|$), and $\mathcal{D}^{(l)}$, $\mathcal{D}^{(g)}$ represent the better group and worse group in $\mathcal{D}$, γ is the top quantile for splitting observations into the better group $\mathcal{D}^{(l)}$ and the worse group $\mathcal{D}^{(g)}$. f^{γ} is the top-γ-quantile metric function value in the set of observations $\mathcal{D}$. The discrete form of surrogate models (7) can be estimated as

$$\begin{cases} p\left(\boldsymbol{x} \mid \mathcal{D}^{(l)}\right) = w_0^{(l)} p_0(\boldsymbol{x}) + \sum_{i=1}^{N^{(l)}} w_i k\left(\boldsymbol{x}, \boldsymbol{x}_i \mid \boldsymbol{b}^{(l)}\right), \\ p\left(\boldsymbol{x} \mid \mathcal{D}^{(g)}\right) = w_0^{(g)} p_0(\boldsymbol{x}) + \sum_{i=N^{(l)}+1}^{N} w_i k\left(\boldsymbol{x}, \boldsymbol{x}_i \mid \boldsymbol{b}^{(g)}\right), \end{cases} \tag{8}$$

where w_i is the weight determined by weighting algorithms at each iteration, k is a kernel function parameterized by the BWs $\boldsymbol{b}^{(l)}$ and $\boldsymbol{b}^{(g)}$, $\boldsymbol{b}^{(l)}$, $\boldsymbol{b}^{(g)}$ are the constant vectors in kernel function (BW of a kernel function), and p_0 is a noninformative prior. For a set of weights $\{w_i\}_{i=1}^{N}$, the weight terms add up to 1 ($w_i \geq 0$).

2) Acquisition Function: The acquisition function is formulated as

$$r(\boldsymbol{x} \mid \mathcal{D}) = \frac{p\left(\boldsymbol{x} \mid \mathcal{D}^{(l)}\right)}{p\left(\boldsymbol{x} \mid \mathcal{D}^{(g)}\right)}, \tag{9}$$

where acquisition function $r(\boldsymbol{x} \mid \mathcal{D})$ is the ratio of the better and worse observations.

Algorithm 1 summarizes the TPE-BO algorithm described by the previous equations

The weighting algorithm adopted in TPE-BO algorithm is designed as [20]

$$w_i = \begin{cases} \frac{1}{N^{(l)}+1} & \left(i = 0, \ldots, N^{(l)}\right) \\ \frac{1}{N^{(g)}+1} & \left(i = N^{(l)}+1, \ldots, N+1\right). \end{cases} \tag{10}$$

Algorithm 1 : TPE-BO Algorithm

1: Initialize $\mathcal{D} \leftarrow \emptyset$;
2: Randomly choose $\boldsymbol{x}_0 \in \mathbb{R}^n$ constrained to $\boldsymbol{x}_l \leq \boldsymbol{x}_0 \leq \boldsymbol{x}_u$, then get $f(\boldsymbol{x}_0)$ from CST;
3: $\mathcal{D} \leftarrow \mathcal{D} \bigcup \{(\boldsymbol{x}_0,\ f(\boldsymbol{x}_0))\}$;
while $i \neq I_{max}$ (I_{max} is the maximal iterations) **do**
  4: Compute $\gamma = \beta_1 \in (0, 1]$;
  5: Split $\mathcal{D}$ into $\mathcal{D}^{(l)}$ and $\mathcal{D}^{(g)}$;
  6: Compute weights $\{w_i\}_{i=1}^{N+1}$ according to (10);
  7: Compute BWs $\boldsymbol{b}^{(l)}$ and $\boldsymbol{b}^{(g)}$ according to (13);
  8: Calculate surrogate models $p\left(\boldsymbol{x} \mid \mathcal{D}^{(l)}\right), p\left(\boldsymbol{x} \mid \mathcal{D}^{(g)}\right)$ by (8);
  9: Sample $\mathcal{S} = \{\boldsymbol{x}_s\}_{s=1}^{N_s} \sim p\left(\boldsymbol{x} \mid \mathcal{D}^{(l)}\right)$;
  10: Pick $\boldsymbol{x}_{i+1} = \boldsymbol{x}^* \in \operatorname{argmax}_{\boldsymbol{x} \in \mathcal{S}} r(\boldsymbol{x} \mid \mathcal{D})$;
  11: Run EM calculations in CST with $\boldsymbol{x}_{i+1}$ and obtain metric function $f(\boldsymbol{x}_{i+1})$;
  12: $\mathcal{D} \leftarrow \mathcal{D} \bigcup \{(\boldsymbol{x}_{i+1},\ f(\boldsymbol{x}_{i+1}))\}$;
end while

And the kernel function is formulated as

$$k(\boldsymbol{x}, \boldsymbol{x}_i) = \frac{g(\boldsymbol{x}, \boldsymbol{x}_i \mid \boldsymbol{b})}{Z(\boldsymbol{x}_i)}, \tag{11}$$

where the truncated Gaussian function $g(\boldsymbol{x}, \boldsymbol{x}_i \mid \boldsymbol{b})$ is designed as

$$\begin{cases} g(\boldsymbol{x}, \boldsymbol{x}_i \mid \boldsymbol{b}) = \dfrac{1}{\sqrt{2\pi \boldsymbol{b}^2}} \exp\left[-\dfrac{1}{2}\left(\dfrac{\boldsymbol{x} - \boldsymbol{x}_i}{\boldsymbol{b}}\right)^2\right] \\ Z(\boldsymbol{x}_i) = \displaystyle\int_{\boldsymbol{x}_l}^{\boldsymbol{x}_u} g(\boldsymbol{x}, \boldsymbol{x}_i \mid \boldsymbol{b})\,. \end{cases} \tag{12}$$

In (12), $Z(\boldsymbol{x}_i)$ is a normalization vector. $\boldsymbol{b}$ (a positive vector) is called BW of kernel function. The BW $\boldsymbol{b}_i$ for i^{th} kernel function is calculated in a heuristic way as

$$\boldsymbol{b}_i = \begin{cases} \boldsymbol{x}_i - \boldsymbol{x}_{i-1} & (\text{ if } \boldsymbol{x}_{i+1} \text{ not exist }), \\ \boldsymbol{x}_{i+1} - \boldsymbol{x}_i & (\text{ if } \boldsymbol{x}_{i-1} \text{ not exist }), \\ \max(\{\boldsymbol{x}_{i+1} - \boldsymbol{x}_i, \boldsymbol{x}_i - \boldsymbol{x}_{i-1}\}) & (\text{otherwise}), \end{cases} \tag{13}$$

where observations $\boldsymbol{x}_i$ satisfies $\boldsymbol{x}_l = \boldsymbol{x}_1 \leq \boldsymbol{x}_2 \leq \cdots \leq \boldsymbol{x}_N = \boldsymbol{x}_u$. It can be observed in (13), the BW $\boldsymbol{b}_i$ depends on the concentration of observations, which means the BW $\boldsymbol{b}_i$ will be larger if observations in a region are fewer meanwhile the BW will be narrower if a region has many observations. Hence, the TPE-BO assisted antenna design framework is shown in Fig. 12.

As illustrated in Fig. 12, the TPE-BO algorithm is utilized for the automatic design of antennas until a satisfactory outcome is achieved. This approach necessitates a co-simulation between the CST and a Python-based solver. During the design phase, given geometric parameters and an initial point, the method predicts feasible geometric parameters iteratively using the Tree-Structured Parzen Estimator and accumulated sample data. The sample dataset expands with each iteration as new data points $(\boldsymbol{x}_{i+1},\ f(\boldsymbol{x}_{i+1}))$ are incorporated into the existing dataset. Consequently, as the dataset grows, TPE-BO increasingly refines its prediction of the antenna's geometric parameters to minimize the objective function.

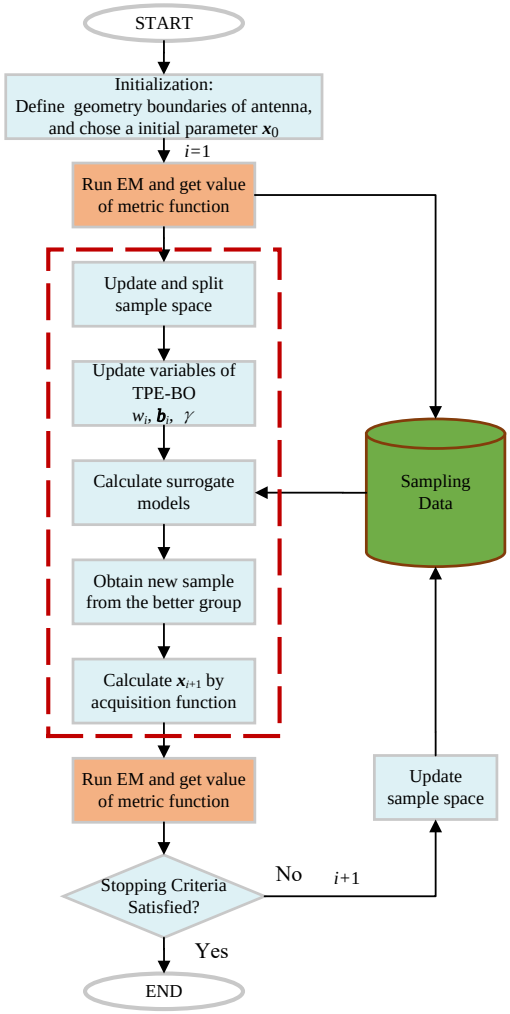

Fig. 12. The TPE-BO assisted antenna design framework.

TPE-BO has several distinct advantages over the optimization methods discussed in this article. 1) High efficiency and faster convergence: TPE-BO is generally more efficient in balancing exploration and exploitation because the probabilistic model helps identify promising regions of the hyperparameter space more quickly than other non-probabilistic methods, and converges rapidly without requiring a large amount of data [17] [24]. 2) Global optimality: TPE-BO's probabilistic nature and segmentation strategy for hyperparameter space significantly reduce the risk of getting stuck in local minima, thus supporting global optimality [19] [20]. 3) Requiring less hyperparameter tuning: TPE-BO requires less tuning of its hyperparameters compared to PSO, which may need careful tuning of population sizes, maximum iterations, the initialization method for setting initial points, etc [19], [20], [37]. 4) Robustness: In addition, TPE-BO has been implemented in several popular machine-learning libraries and frameworks, such as Hyperopt and Optuna. Its robustness has been validated in practice on numerous applications and datasets [38].

Based on these advantages, this paper employs the TPE-BO design framework to explore the optimal BW of the proposed hybrid dipole antenna.

C. Antenna Exploration Based on TPE-BO Algorithm Optimization Framework

In the optimization process of TPE-BO, the computational budget was 1200 electromagnetic (EM) simulations. All other TPE-BO settings follow the default configuration of the previously discussed optimization algorithm. Through three complete TPE-BO algorithm runs satisfactory design results can be obtained with an average of 700 EM simulations. The best design is shown in Table II. The optimal BW is in the range of 1.62 to 4.22 GHz. The coupling between the two ports is less than -21 dB within the operational bands. Compared to CST's optimizer, the TPE-BO shows an increase in BW of 1.55 and 1.42 GHz over CST's TRF and PSO algorithms, respectively, demonstrating its excellent global optimization capability, as shown in Fig. 13.

Meanwhile, according to the reflection coefficients comparison between Model A, Model B, and a hybrid antenna incorporating an optimized HDL structure, as shown in Fig. 1, it is demonstrated that the goal of achieving a low-profile, wideband dipole antenna can be efficiently and rapidly achieved by employing an HDL structure alongside the TPE-BO algorithm, without modifying the original structure and size of the single petal-shaped antenna. Notably, this methodology significantly improves the BW (within the reflection coefficient below -13 dB) from 22.5% to 89% while reducing the antenna's profile from 0.2 λ_L to 0.1 λ_L compared to the single petal-shaped antenna, where λ_L represents the wavelength at the lowest frequency within the operational BW. This advancement underscores the critical role of the HDL structure in improving antenna performance and provides a novel, balanced and effective approach to achieving more efficient and compact antenna designs.

However, it should be noted that the total efficiency of the hybrid antenna decreases at high frequencies, as shown in Fig. 15. The total efficiency decline is primarily due to the high loss tangent of the selected HDL structural material (loss tangent = 0.018), rather than the proposed framework. The total efficiency can be improved by replacing the HDL structural material with one that has a permittivity of 12 and a loss tangent of 0.003, produced by the same company. By optimizing the HDL structure, a reflection coefficient of less than -12.5 dB from 1.58 GHz to 4.12 GHz and a total efficiency greater than 88% across the entire operating frequency band are achieved, as shown in Fig. 15. This proves the effectiveness of the proposed framework in improving the dipole antenna performance in this article.

The BW, coupling, and realized gain performance of TPE-BO meet the optimization objectives of this study, confirming the practicality of the proposed dipole antenna with HDL structure for physical realization, including prototyping and manufacturing.

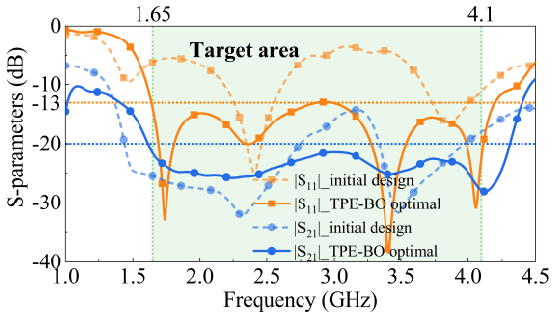

Fig. 13. The optimal results of the TPE-BO based antenna optimization algorithm.

TABLE II
OPTIMAL RESULTS OF THE DIPOLE ANTENNA WITH A 10-LAYER HDL

RESULTS	WEIGHT	TPE-BO	PSO	TRF
MAX$\|S_{11}\|$ (dB)	0.5	-12.9	-10.2	-10.1
MAX$\|S_{21}\|$ (dB)	0.25	-21.4	-20.3	-18.3
MINIMUM REALIZED GAIN IN-BAND (dBi)	0.25	5	5	5
BW (GHz) $\|S_{11}\| \leq -13dB$	/	1.62 - 4.22	1.66 - 2.82	1.65-2.68
AVERAGED TIME (ALGORITHM + EM SIMULATION) (MIN)	/	13.1	15.2	13.2
AVERAGE NUMBER OF CONDUCTED EM SIMULATIONS	/	700	1200	1200

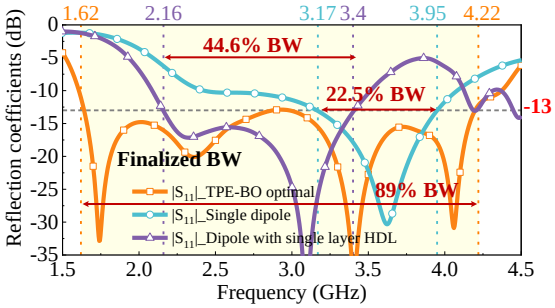

Fig. 14. Reflection coefficients of the single petal-shaped antenna (Model A), single petal-shaped antenna with single layer HDL (Model B), and petal-shaped antenna with an optimized HDL structure.

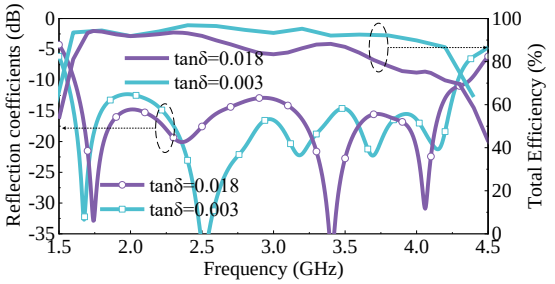

Fig. 15. Comparison of reflection coefficients and total efficiency for different HDL materials.

IV. EXPERIMENTAL IMPLEMENTATION AND VALIDATION

To validate the effectiveness of reducing the antenna profile and increasing the BW using HDL structures, a petal-shaped dipole antenna with an optimized HDL structure, as optimized by the TPE-BO algorithm in Sec. III, was fabricated and characterized. The optimized HDL structure, shown in Fig. 16(b), was 3D printed using a commercial Raise3D Pro2 printer with Fused Filament Fabrication (FFF) technology, which has a high-resolution printing accuracy of 0.01 mm. In addition, the printed filaments are baked in a 90°C oven for 4.5

TABLE III
COMPARISON OF THE PROPOSED LOW-PROFILE AND BROADBAND DIPOLE ANTENNA AND OTHERS

REF.	PROFILE(λ_L)	AREA(λ_L^2)	VSWR	FBW (BW/GHZ)	EXTRA FEEDING NETWORK	PEAK GAIN (dBi)	BROADBAND LOW PROFILE WITHOUT DIPOLE CHANGE
[6]	0.14	0.59×0.59	≤ 2	48.3% (1.68-2.75)	YES	9.6	NO
[7]	0.19	0.74×0.74	≤ 2	44.9% (1.33-2.1)	NO	7.7	NO
[8]	0.12	0.51×0.51	≤ 2	46.4% (1.69-2.71)	NO	9.8	NO
[9]	0.09	0.46×0.46	≤ 2	40% (3-4.5)	YES	7.2	NO
[10]	0.35	0.71×0.71	≤ 1.5	64.7% (1.4–2.77)	YES	9	NO
[11]	0.2	0.48×0.48	≤ 1.6	40.5% (3.38-5.1)	YES	7.5	NO
[12]	0.11	0.88×0.88	≤ 1.46	34.5% (3.6-5.1)	NO	11.5	NO
PRO.	0.1	0.58×0.58	≤ 1.6	79% (1.62-3.75)	NO	10.2	YES

Remark: λ_L is the free space wavelength of the lowest frequency of the optional band; and FBW refers to the measured overlap BW between -10 dB S11 BW and 3 dB gain BW.

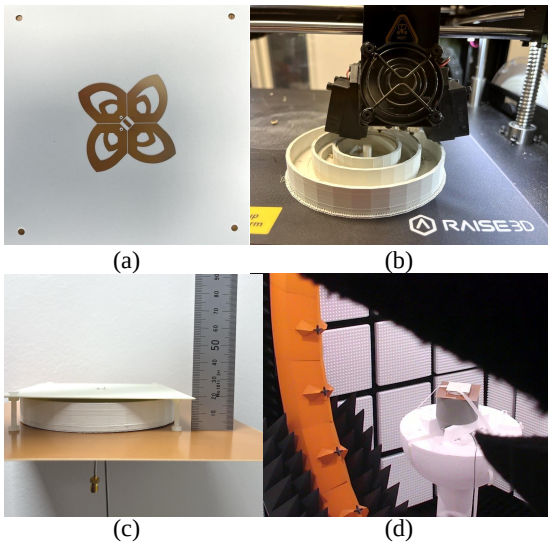

Fig. 16. Prototype of the proposed low-profile broadband antenna, (a) the bottom of the fabricated dipole antenna, (b) the 3D printing process of the proposed 10-layer HDL structure, (c) the assembled proposed antenna, and (d) the anechoic chamber measurement.

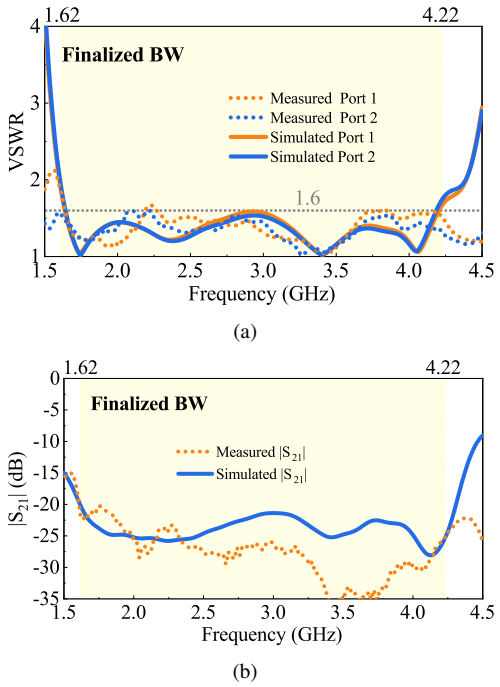

Fig. 17. Measured and simulated (a) VSWRs and (b) isolation of the proposed antenna.

hours before printing to dehumidify the material and improve surface quality. Some of the important setup parameters during printing are as follows: nozzle temperature of 300°C, infill density of 100%, infill flowrate of 115%, and heated bed temperature of 100°C. The dimensions of the 3D printed white HDL structure are 109.8 mm × 109.8 mm × 18 mm. The HDL structure was attached to the ground plane using a minimal amount of Loctite Super Glue. The final assembly is shown in Fig. 16(c).

The radiation performance and S-parameters of the fabricated antenna prototype were fully tested using the SATIMO SG24L spherical near-field scanner and the KEYSIGHT N5227A PNA vector network analyzer, respectively. As shown in Fig. 17, the measured VSWRs for Port 1 and Port 2 are $\leq$1.6 over the frequency range of 1.62 to 4.22 GHz, which aligns with the simulated results. The VSWR of Port 1 is slightly higher than that of Port 2 due to the use of via configurations in Port 1 to avoid overlap but still demonstrates satisfactory performance. The measured minimum isolation $|S_{21}|$ exceeds 20.5 dB. The measured realized gain, depicted in Fig. 18, ranges from 5 to 10.2 dBi with peaks at 4 GHz. Consequently, the final measured overlap BW (FBW) between the -10 dB S11 BW and the 3 dB gain BW is from 1.62 GHz to 3.75 GHz (79.3%). The increase in realized gain at high frequencies is due to the excitation of the higher-order modes of the DR at high frequencies, which can effectively increase the realized gain [29] [31]. The measured total efficiency ranges from 64% to 87.5%. The measured total efficiency of the antenna drops significantly after 3.4 GHz compared

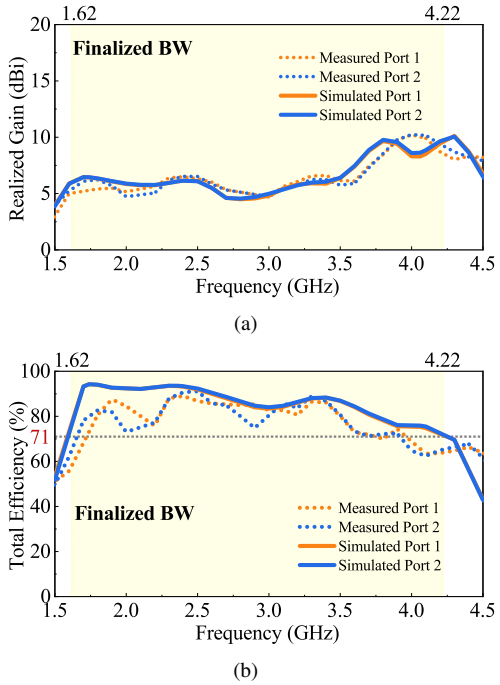

Fig. 18. Measured and simulated (a) gain and (b) Total efficiency of the proposed antenna.

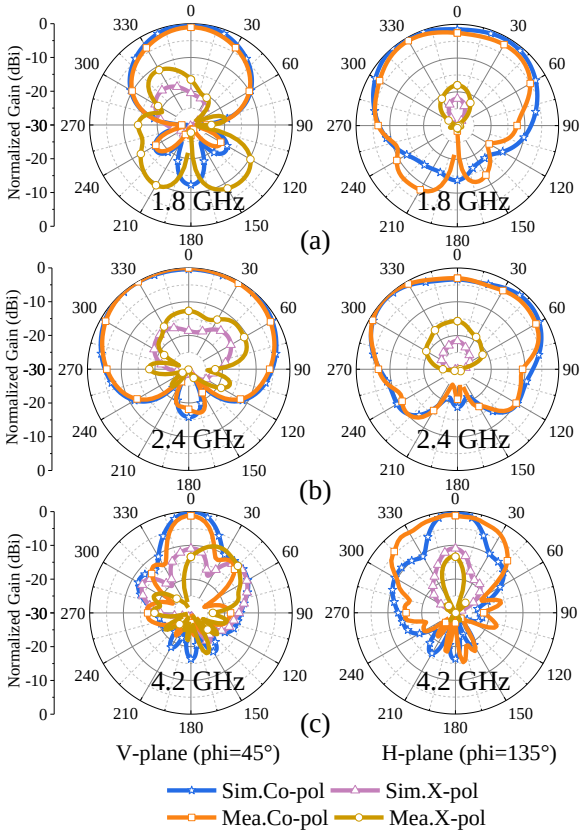

Fig. 19. Simulated and measured radiation patterns of port1 in V-plane and H-plane. (a) 1.8 GHz; (b) 2.4 GHz; (c) 4.2 GHz.

to the simulated results, which is attributed to the actual loss tangent of the HDL material being higher than the simulated setting of 0.018 at higher frequencies, as shown in Fig. 3. The issue of the reduction in total efficiency from 3.4-4.22 GHz observed in both the measured and simulated results can be addressed by using materials with a lower loss tangent to construct the HDL structure, as discussed in Section III-C. Fig. 19 shows measured and simulated co-polarized and cross-polarized radiation patterns in the V-plane (phi=45 degrees) and H-plane (phi=135 degrees) at 1.8 GHz, 2.4 GHz and 4.2 GHz, respectively. In addition to the effects caused by the variation of the HDL's loss tangent with frequency and traditional errors such as cable loss, SMA connector issues, and soldering techniques, discrepancies between simulated and measured results can also be attributed to the manual sanding required during the post-processing of the HDL structure created by 3D printing. The precision of this sanding affects the height of the HDL structure. In addition, irregularities at the base of the HDL, even with less Loctite Super Glue, create significant air gaps between the HDL and the ground plane, as shown in Fig. 16(c), causing loss and interference during testing.

To illustrate the superiority of the proposed HDL structure in enhancing both BW and compactness, Table III compares the performance of the proposed broadband, low-profile, dual-polarized dipole antenna with other reported designs. The proposed method provides ultrawideband performance with efficient impedance matching (VSWR$\leq$1.6) while enabling a compact design without the need for an additional matching feed network. Meanwhile, in contrast to methods described in the literature for achieving both wide BW and compactness, which often inevitably affect the performance of the original dipole antenna and complicate fabrication processes, the HDL structure proposed in this study offers a streamlined solution. By simply adjusting the height and radius of the HDL structure, it is possible to improve both BW and profile without making any changes to the original dipole antenna. In addition, a fully automated, rapid design framework for low-profile, broadband dipole antennas is realized through the application of TPE-BO optimization algorithms. This approach simplifies antenna design, reduces time and cost, and has great potential for advanced wireless communications.

V. Conclusion

This paper presents a method for quickly and simultaneously achieving excellent impedance matching over an extensive BW by simply incorporating the HDL structure beneath a dipole antenna. The fundamental operating principle of the method to achieve low profiles and wide BW is also explained. Prototypes were fabricated and tested to verify the feasibility of the proposed method and to demonstrate the exceptional ultrawideband capabilities of the antenna. The prototype has a compact size of $0.58\lambda_L \times 0.58\lambda_L \times 0.1\lambda_L$ and achieves a wide overlap BW between the impedance matching BW and the 3 dB gain BW of 79.3% (from 1.62 to 3.75 GHz) with a VSWR threshold below 1.6. Moreover, the application of the TPE-BO algorithm introduces a streamlined, automated design

framework that considerably reduces the complexity, time, and cost of antenna design.

The novel strategy presented in this work not only simplifies the antenna design and fabrication process but also provides a viable solution for realizing compact wideband antennas with significant potential for wireless systems.

ACKNOWLEDGMENTS

Alessandro Tibo is now working at AstraZeneca AB R&D, Gothenburg.

REFERENCES

[1] N. Liu, S. -W. Qu and S. Yang, "Dual-Polarized Phased Array With Ultralow Profile for Wide-Angle Scanning Application," *IEEE Antennas Wireless Propag. Lett*., vol. 23, no. 2, pp. 613-617, Feb. 2024.

[2] T. H. Brandão and A. Cerqueira S., "Triband Antenna Array for FR1/FR2 5G NR Base Stations," *IEEE Antennas Wireless Propag. Lett*., vol. 22, no. 4, pp. 764-768, Apr. 2023.

[3] S. Hussain, S. -W. Qu, P. Zhang, X. -H. Wang and S. Yang, "A Low-Profile, Wide-Scan, Cylindrically Conformal X-Band Phased Array," *IEEE Antennas Wireless Propag. Lett*., vol. 20, no. 8, pp. 1503-1507, Aug. 2021.

[4] Z. H. Jiang, D. E. Brocker, P. E. Sieber and D. H. Werner, "A Compact, Low-Profile Metasurface-Enabled Antenna for Wearable Medical Body-Area Network Devices," *IEEE Trans. Antennas Propag*., vol. 62, no. 8, pp. 4021-4030, Aug. 2014.

[5] Y. Sun, J. Zhang, P. Mei, S. Luo, W. Fu and S. Zhang, "Tri-Band Dual-Polarized Shared-Aperture Antenna Arrays With Wide-Angle Scanning and Low Profile for 5G Base Stations," *IEEE Trans. Antennas Propag*., vol. 72, no. 3, pp. 2455-2467, Mar. 2024.

[6] Z. Zhou, Z. Wei, Z. Tang and Y. Yin, "Design and Analysis of a Wideband Multiple-Microstrip Dipole Antenna with High Isolation," *IEEE Antennas Wireless Propag. Lett*., vol. 18, no. 4, pp. 722-726, Apr. 2019.

[7] W. Yang and Y. Pan, "A Wideband Dual-Polarized Dipole Antenna With Folded Metallic Plates," *IEEE Antennas Wireless Propag. Lett*., vol. 17, no. 10, pp. 1797-1801, Oct. 2018.

[8] S. S. Syed Nasser and Z. N. Chen, "Low-Profile Broadband Dual-Polarization Double-Layer Metasurface Antenna for 2G/3G/LTE Cellular Base Stations," *IEEE Trans. Antennas Propag*., vol. 70, no. 1, pp. 75-83, Jan. 2022.

[9] M. -S. Liang, Y. Zhou, X. -S. Yang and P. -F. Wu, "A Low-Profile Dual-Polarized Substrate Integrated Magneto-Electric Dipole MIMO Antenna," *IEEE Antennas Wireless Propag. Lett*., vol. 22, no. 6, pp. 1431-1435, Jun. 2023.

[10] L. H. Ye, X. Y. Zhang, Y. Gao and Q. Xue, "Wideband Dual-Polarized Four-Folded-Dipole Antenna Array With Stable Radiation Pattern for Base-Station Applications," *IEEE Trans. Antennas Propag*., vol. 68, no. 6, pp. 4428-4436, Jun. 2020.

[11] Y. Qin, L. Zhang, C. -X. Mao and H. Zhu, "A Compact Wideband Antenna With Suppressed Mutual Coupling for 5G MIMO Applications," *IEEE Antennas Wireless Propag. Lett*., vol. 22, no. 4, pp. 938-942, Apr. 2023.

[12] B. Wang, C. Liao and C. -H. Du, "A Low-Profile Broadband Dual-Polarized Base Station Antenna Array With Well-Suppressed Cross-Polarization," *IEEE Trans. Antennas Propag*., vol. 69, no. 12, pp. 8354-8365, Dec. 2021.

[13] J. Zhang, M. O. Akinsolu, B. Liu and S. Zhang, "Design of Zero Clearance SIW Endfire Antenna Array Using Machine Learning-Assisted Optimization," *IEEE Trans. Antennas Propag*., vol. 70, no. 5, pp. 3858-3863, May 2022.

[14] F. Andriulli, P.-Y. Chen, D. Erricolo, and J.-M. Jin, "Guest Editorial Machine Learning in Antenna Design, Modeling, and Measurements," *IEEE Trans. Antennas Propag.*, vol. 70, no. 7, pp. 4948-4952, Jul. 2022.

[15] J. Zhou, Z. Yang, Y. Si, L. Kang, H. Li, M. Wang, and Z. Zhang, "A Trust-Region Parallel Bayesian Optimization Method for Simulation-Driven Antenna Design," *IEEE Trans. Antennas Propag.*, vol. 69, no. 7, pp. 3966-3981, Jul. 2021.

[16] F. Peng and X. Chen, "An Efficient Antenna Optimization Framework Based on the NP to P Problem," *IEEE Trans. Antennas Propag.*, vol. 72, no. 6, pp. 4818-4828, Jun. 2024.

[17] Y. Zeng, X. Qing, and M. Y.-W. Chia, "A Wideband Circularly Polarized Antenna with a Nonuniform Metasurface Designed via Multiobjective Bayesian Optimization," *IEEE Antennas Wireless Propag. Lett.*, vol. 23, no. 6, pp. 1739-1743, Jun. 2024.

[18] B. Liu, H. Aliakbarian, Z. Ma, G. A. E. Vandenbosch, G. Gielen and P. Excell, "An Efficient Method for Antenna Design Optimization Based on Evolutionary Computation and Machine Learning Techniques," *IEEE Trans. Antennas Propag.*, vol. 62, no. 1, pp. 7-18, Jan. 2014.

[19] S. Watanabe, "Tree-Structured Parzen Estimator: Understanding Its Algorithm Components and Their Roles for Better Empirical Performance," 2023, arXiv preprint arXiv:2304.11127, [Online]. Available: https://arxiv.org/abs/2304.11127.

[20] J. Bergstra, R. Bardenet, Y. Bengio, and B. Kégl, "Algorithms for hyper-parameter optimization," in *Advances in Neural Information Processing Systems*, vol. 24, 2011.

[21] S. Koziel and A. Pietrenko-Dabrowska, "Reduced-cost electromagnetic-driven optimisation of antenna structures by means of trust-region gradient-search with sparse Jacobian updates," *IET Microw. Antennas Propag.*, vol. 13, no. 10, pp. 1646-1652, Aug. 2019.

[22] J. Kennedy and R. Eberhart, "Particle swarm optimization," *Proc. of ICNN'95 - Int. Conf. on Neural Networks*, Perth, WA, Australia, 1995, pp. 1942-1948.

[23] Z. D. Zaharis et al., "Exponential Log-Periodic Antenna Design Using Improved Particle Swarm Optimization With Velocity Mutation," *IEEE Trans. Magnetics*, vol. 53, no. 6, Art no. 7204104, pp. 1-4, Jun. 2017.

[24] M. Benzaghta, G. Geraci, D. López-Pérez, and A. Valcarce, "Designing Cellular Networks for UAV Corridors via Bayesian Optimization," *Proc. of GLOBECOM 2023 - 2023 IEEE Global Communications Conference*, 2023, pp. 4552-4557.

[25] Avient, "ABS1500 TP21559 Technical Datasheet," Avient. [Online]. Available: https://www.avient.com/products/engineered-polymer-formulations/conductive-signal-radiation-shielding-formulations/preperm-low-loss-dielectric-thermoplastics.

[26] SPEAG, "DAK-TL-2 Dielectric Assessment Kit," SPEAG. [Online]. Available: https://speag.swiss/products/dak/dak-tl-2/.

[27] C. A. Balanis, "Wave Propagation and Polarization," in *Advanced Engineering Electromagnetics*, 2nd ed., New York, NY, USA: Wiley, 2012, Ch. 4, Sec. 3, pp. 142.

[28] C. A. Balanis, "Circular Cross-Section Waveguides and Cavities," in *Advanced Engineering Electromagnetics*, 2nd ed., New York, NY, USA: Wiley, 2012, Ch. 9, sec. 5, pp. 527.

[29] D. Li, L. Shi, J. Wang, Y. Liu and Q. Chen, "High-Gain Wideband Dielectric Resonator Antenna Based on Semi-Cylindrical Grooved Structure," *IEEE Trans. Circuits Syst. II: Exp. Briefs*, vol. 71, no. 3, pp. 1101-1105, Mar. 2024.

[30] M. -D. Yang, Y. -M. Pan, Y. -X. Sun and K. -W. Leung, "Wideband Circularly Polarized Substrate-Integrated Embedded Dielectric Resonator Antenna for Millimeter-Wave Applications," *IEEE Trans. Antennas Propag.*, vol. 68, no. 2, pp. 1145-1150, Feb. 2020.

[31] S. Varghese, P. Abdulla, A. M. Baby and J. P. M., "High-Gain Dual-Band Waveguide-Fed Dielectric Resonator Antenna," *IEEE Antennas Wireless Propag. Lett.*, vol. 21, no. 2, pp. 232-236, Feb. 2022.

[32] Y. Li, F. Wu, D. Xi, Z. Jiang, C. Yu and W. Hong, "A Millimeter-Wave Wideband Dual-Polarized Integrated DRA Array with Improved Isolation," *IEEE Antennas Wireless Propag. Lett.*, vol. PP, no. 1, pp. 1-5, Jan. 2024.

[33] T. Yang, J. Ren, B. Zhang, Y. -T. Liu, T. Ma and Y. Yin, "Wideband Diversity Cylindrical Dielectric Resonator Antenna Based on Multimode Resonance," *IEEE Antennas Wireless Propag. Lett.*, vol. 22, no. 9, pp. 2205-2209, Sept. 2023.

[34] F. Peng and X. Chen, "An Efficient Optimization Method for Antenna Arrays Using a Small Population Diploid Genetic Algorithm Based on Local RBF Networks," *IEEE Trans. Antennas Propag.*, vol. 72, no. 4, pp. 3237-3249, April 2024.

[35] J. Tan, Y. Shao, J. Zhang and J. Zhang, "Efficient Antenna Modeling and Optimization Using Multifidelity Stacked Neural Network," *IEEE Trans. Antennas Propag.*, vol. 72, no. 5, pp. 4658-4663, May 2024.

[36] L. Song, B. Zhang, D. Zhang and Y. Rahmat-Samii, "Embroidery Electro-Textile Patch Antenna Modeling and Optimization Strategies With Improved Accuracy and Efficiency," *IEEE Trans. Antennas Propag.*, vol. 70, no. 8, pp. 6388-6400, Aug. 2022.

[37] M. Clerc and J. Kennedy, "The particle swarm - explosion, stability, and convergence in a multidimensional complex space," *IEEE Trans. Evol. Comput.*, vol. 6, no. 1, pp. 58-73, Feb. 2002.

[38] S. Shekhar, A. Bansode, and A. Salim, "A Comparative Study of Hyper-Parameter Optimization Tools," *Proc. 2021 IEEE Asia-Pacific Conf. on Computer Science and Data Engineering (CSDE)*, pp. 1-6, 2021.

Ying Sun received the B.E. degree from Southwest Petroleum University, Chengdu, China, in 2017, and the M.S. degree from the University of Electronic Science and Technology of China, Chengdu, China, in 2020. She is currently pursuing the Ph.D. degree in the Antennas, Propagation and Millimeter-wave Systems (APMS) Section with the Department of Electronic Systems, Aalborg University, Aalborg, Denmark. Her current research interests include wideband antennas, dual-polarized, shared-aperture antennas, and arrays.

Jin Zhang received the B.E. degree from the University of Electronic Science and Technology of China, Chengdu, China, in 2012 and the Ph.D degree in millimeter-wave antennas for 5G mobile terminals and base stations from Aalborg University, Aalborg, Denmark, in 2020. During the study of the Ph.D, she was a visiting researcher at Aalto University, Espoo, Finland. She was a research assistant and postdoctoral researcher in Aalborg University from 2020 to 2022. Her research interests include mm-wave, dual-polarized, shared aperture antennas and arrays.

Alessandro Tibo receives his PhD in Smart Computing from the University of Florence in 2019. Following this, he pursued an academic career from 2019 to 2022 in the Department of Computer Science at Aalborg University (AAU), initially as a postdoc and later as an Assistant Professor. During his time at AAU, he started this project and contributed to the framework idea. Since 2022, he has been employed as scientist at AstraZeneca AB R&D, Gothenburg, Sweden, where he develops generative machine learning models for de novo drug design.

Peyman Aghabeyki was born in Mazandaran Province, Iran in 1993. He received a BSc degree in electrical engineering from Nooshirvani University of Technology, Babol, Iran, in 2016 and an MSc in Telecommunication Engineering, Field and waves with a focus on SIW antennas from the Amirkabir University of Technology, Tehran, Iran in 2019. He is currently pursuing a Ph.D. degree in the Antennas, Propagation, and Millimeter-wave Systems (APMS) section, at the Department of Electronic Systems, Aalborg University, Aalborg, Denmark. His main research interests include Liquid Crystal-based Reflectarrays and antennas for millimeter-wave applications and Base-station antennas.

Zhaohui Wei was born in Shandong, China. He received the B.Sc. and M.Eng. degrees in electronic engineering from Xidian University, Xi'an, China, in 2017 and 2020, respectively. He is currently pursuing a Ph.D. degree with the Antennas, Propagation and Millimeter-Wave Systems Section, Department of Electronic Systems, Aalborg University, Aalborg, Denmark. His research interests include filtering antenna, frequency selective surface, and deep-learning-based methods for the design and analysis of antenna systems. In 2023, he visited the University of Alcala, Spain for 3 months. In 2024, he joined Xidian University as an associate professor.

Shengyuan Luo received the B.E. and M.S. degrees from Harbin Engineering University in 2015 and 2019, respectively. He received the PhD degree in Aalborg University, Denmark in 2023. He is currently working with Anhui University. His recent research interests include microstrip antennas, wideband antennas, millimeter-wave array antennas, and massive MIMO antenna arrays, filter antenna, share aperture antenna.

Shuai Zhang received the B.E. degree from the University of Electronic Science and Technology of China, Chengdu, China, in 2007 and the Ph.D. degree in electromagnetic engineering from the Royal Institute of Technology (KTH), Stockholm, Sweden, in 2013. In 2014, he joined Aalborg University, Denmark, where he is currently a Full Professor and the Head of Antenna Research Group. In 2010 and 2011, he was a Visiting Researcher at Lund University, Sweden and at Sony Mobile Communications AB, Sweden, respectively. He was also an external antenna specialist at Bang & Olufsen, Denmark from 2016-2017. He has supervised/co-supervised 10 Postdocs and 18 PhD students. He has coauthored over 130 articles in well-reputed international journals and over 17 US or WO patents. His citations in Scopus are over 5300 with H index of 38. His current research interests include: millimeter-wave antennas for cellular communications, bio-electromagnetics, metasurfaces, CubeSat antennas, Massive MIMO antennas, wireless sensors, and RFID antennas.

He is the Associate Editor for IEEE Antennas and Wireless Propagation Letters; Sensors; and IET Microwaves, Antennas and Propagation. He is also a reviewer for all the top IEEE and IET journals in antenna areas, where he got the prize of "Top Reviewers in IEEE Transactions on Antennas and Propagation 2019-2020 and 2020-2021". He is the General Co-Chair for iWAT2023 at Aalborg, Denmark, the Super Reviewer (previously known as Super TPC or Vice Chair) for IEEE APS 2020 and 2021 and the TPC for several top IEEE conferences. He is the recipient of "IEEE Antennas and Propagation Society Young Professional Ambassador" in 2022, where he gives presentation for different IEEE Chapters on Antennas for Mobile Communications. He has also been intensively invited to international conference and industry to give keynote/plenary speech and presentations. From 2024, he has been the European Association on Antennas and Propagation (EurAAP) Regional Delegate.